Engineering and Tuning of Quantum Emitters in Few-Layer Hexagonal Boron Nitride

Noah Mendelson[+], Zai-Quan Xu[+]*, Toan Trong Tran[+], Mehran Kianinia[+] John Scott[+], Carlo Bradac[+], Igor Aharonovich[+]* and Milos Toth[+]*

[+] *Institute of Biomedical Materials and Devices, Faculty of Science, University of Technology Sydney, Ultimo, New South Wales, 2007, Australia*
* zaiquan.xu@uts.edu.au, igor.aharonovich@uts.edu.au, milos.toth@uts.edu.au

Abstract
Quantum technologies require robust and photostable single photon emitters (SPEs). Hexagonal boron nitride (hBN) has recently emerged as a promising candidate to host bright and optically stable SPEs operating at room temperature. However, the emission wavelength of the fluorescent defects in hBN has, to date, been shown to be uncontrolled, with a wide spread of zero phonon line (ZPL) energies spanning a broad spectral range (hundreds of nanometers), which hinders the potential development of hBN-based devices and applications. Here we demonstrate chemical vapor deposition growth of large-area, few-layer hBN films that host large quantities of SPEs: ~100–200 per 10×10 µm^2. More than 85% of the emitters have a ZPL at (580 ± 10) nm, a distribution that is an order of magnitude narrower than reported previously. Furthermore, we demonstrate tuning of the ZPL wavelength using ionic liquid devices over a spectral range of up to 15 nm—the largest obtained to date from any solid state SPE. The fabricated devices illustrate the potential of hBN for the development of hybrid quantum nanophotonic and optoelectronic devices based on 2D materials.

Solid-state, single photon emitters (SPEs) are fundamental hardware components for scalable quantum photonics with proposed applications in quantum cryptography, quantum repeater technologies and entanglement distribution.[1-5] In the past few years, major advances have been achieved in the characterization of single defects in wide-bandgap materials,[1,2,4] as well as single molecules,[6] quantum dots,[3] carbon nanotubes,[7] and more recently layered van der Waals materials.[4,8-11] However, one of the overarching challenges across all platforms is the inability to readily engineer large area (centimeter-scale) materials with uniform spatial and spectral distributions of SPEs. Such a platform is highly desirable for scalable quantum photonic architectures.

To tackle this challenge, two-dimensional (2D) materials which can be fabricated by chemical vapor deposition (CVD) are highly advantageous.[12] They can be grown at low cost, using conventional furnaces and precursors, over large areas. However, to date, 2D materials synthesized *via* this method have not been shown to possess high enough densities of SPEs to be desirable for scalable, integrated technologies. The fabrication of quantum emitter arrays has been pursued by positioning exfoliated flakes on top of lithographically-predefined pillars.[13-15] This process is expensive as it requires e-beam lithography and a subsequent reactive ion-etching

step; the size of the 2D material is also limited due to the exfoliation process resulting in smaller flakes.

Here we demonstrate that these limitations are overcome by bottom-up fabrication of hBN using low-pressure chemical vapor deposition (LPCVD). The technique yields large area (centimeter-scale), high-quality hBN films that host a high density of bright and photostable SPEs. The method stands out in terms of scalability and low cost—which are especially desirable for the engineering of integrated devices based on SPEs in 2D materials.[16-20] The as-grown hBN SPEs exhibit a narrow, uniform distribution of ZPLs, which makes it attractive for device integration. We demonstrate this by implementing an electrostatic tuning method for the emitters employing an ionic liquid technique, and elucidate the tuning mechanism. Employing the SPEs in few nanometer hBN we are able to achieve tuning of over 15 nm at room temperature, the largest reported to date.[21-23]

Results/Discussion
Figure 1a shows a schematic illustration of our growth setup (further details, figure S1 and S2). Briefly, the growth was performed in a quartz tube furnace using ammonia borane (BH_3NH_3) as a precursor, at a temperature of 1030 ˚C, with Ar/H_2 as a carrier gas. Notably, the conditions utilized a very low partial pressure of H_2 gas ~0.05%, and a relatively low gas flow rate of 50 sccm during growth. These conditions (*cf.* Methods) yield high-quality, uniform hBN films (typically less than 10 monolayers) over length scales greater than a cm, and we believe that larger area, up to wafer scale, can be achieved with a bigger tube. An optical image of a hBN film on a Si/SiO_2 substrate is shown in figure 1b, and a scanning electron microscope (SEM) image of the hBN film is shown in figure 1c. Periodic wrinkles and grain boundaries are visible—which is typical of hBN grown by CVD.[20,24] The thickness of the films was determined by AFM (figure 1d) and shown to be 1.4 nm for this particular growth, corresponding to a stack of three-to-four monolayers of hBN. Additionally, sample thickness and film uniformity is shown to be consistent across the sample (figure S3), which was confirmed by analyzing three film edges, each spatially separated by a few millimeters, all of which were found to fall within the range 1.4–2.7 nm, and displayed similar roughness values. The high quality of the as-grown hBN was confirmed by Raman (figure 1e) and Fourier-transform infrared (FTIR) spectroscopy (figure S4). A Raman peak centered at 1369 cm^{-1} is clearly visible, which is characteristic of the E_{2g} mode of few-layer hBN, while the peak at 822 cm^{-1} in the IR spectrum is attributed to the longitudinal optical (LO) A_{2u} vibrational mode.[25]

To perform further optical characterization, the as-grown hBN was transferred to a SiO_2/Si substrate using a polymer-assisted wet transfer technique (*cf.* Methods). In contrast to prior reports,[8-10,26,27] post-growth annealing was not necessary to activate or stabilize the quantum emitters. The optical properties of the emitters were studied at room temperature using a lab-built scanning confocal microscope with a 532-nm excitation laser (*cf.* Methods). The collected emission was filtered using a 568-nm long pass filter, allowing for the observation of hBN emitters at longer wavelengths. Figure 2a displays a histogram of the emission ZPLs measured for 248 individual narrow-band emitters at room temperature. The inset is an example of a single photon emitter with a ZPL at 573 nm, and its corresponding $g^2(\tau)$ measurement confirming single photon emission. All emitters display a phonon sideband located approximately 165 meV below the ZPL energy. More than 85% of the emitters were measured to have their ZPL

wavelength localized in a narrow spectral window, (580 ± 10) nm, and up to 56% in the narrower spectral window (580 ± 5) nm. Such a narrow wavelength distribution constitutes an order of magnitude improvement in the spectral localization of hBN defect emission, which is typically reported to span over two hundred nanometers in the current literature.[9,10]
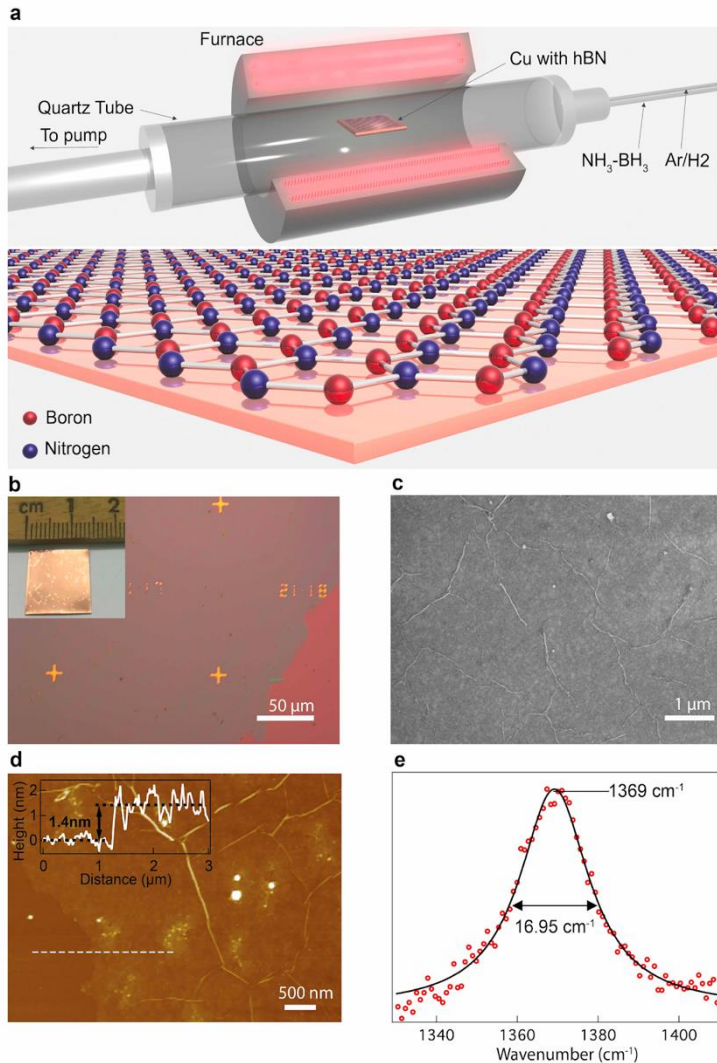
Figure 1 | LPCVD growth and material properties of hBN films. a. *Schematics of LPCVD setup and hBN film on copper. Ammonia borane is used as a CVD precursor. **b.** Optical image of the as-grown hBN film transferred onto a Si/SiO$_2$ substrate marked with gold numbers, showing uniformity of the film. Inset: photograph of the hBN film on copper substrate prior to transfer, showing the cm^2-scale growth area. **c.** An SEM image showing the morphology of the hBN domains transferred onto the Si/SiO$_2$ substrate. **d.** An AFM image of the hBN film on the Si/SiO$_2$ substrate. Inset: height profile of hBN film edge extracted from the white dash line, showing a 1.4-nm step, corresponding to ~3 atomic layers of hBN. **e.** Raman spectrum of the hBN film displaying the characteristic E$_{2g}$ mode measured using an excitation wavelength of 633 nm.*

Importantly, the obtained narrow distribution is consistently reproducible over multiple growths, and was observed in every growth performed at these conditions (*cf.* Methods). Figure 2b shows similar ZPL wavelength distributions—centered on 580 nm—of single emitters measured in hBN samples grown on copper in five separate growths, using nominally identical conditions. To investigate whether the catalytic decomposition of amino-borane on copper plays a role in the observed narrow ZPL distribution by energetically favoring a certain type of defect formation, we also performed growths using nickel and iron foils as growth substrates, keeping all other parameters the same. We found that on all three metals the preferential formation of defects with a ZPL in the range of (580 ± 10) nm is observed. This shows that the underlying process that yields SPEs in this spectral region is robust and suggests that it is not related to catalytic processes at the substrate surface. Figure 2c shows an example of spectra recorded from hBN on each substrate. The observed localization suggests the preferential formation of a particular structural defect, however, the structural nature of this defect remains unclear.
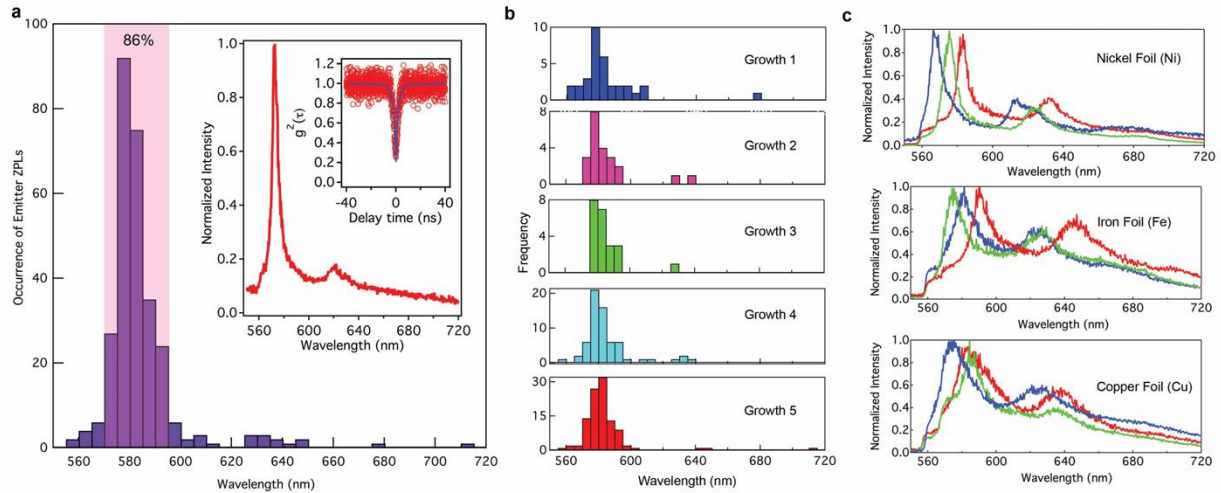

Figure 2 | Spectral distribution of emitters in CVD-grown hBN. a. Histogram of hBN ZPL wavelengths produced using a bin size of 5 nm. A total of 248 emitters from five different hBN films (i.e., growths) were used to generate the histogram. The shaded area highlights the range (580 ± 10) nm, which contains 86% of the emitters. Inset: characteristic room-temperature emission profile of an emitter grown on Cu but transferred to a Si/SiO$_2$ substrate, and corresponding g^2(τ) measurement. b. Individual ZPL distribution histograms from five different growths with nominally identical experimental parameters, showing the robust and reproducible ZPL localization achieved by the LPCVD growth technique (bin size = 5 nm). c. Three representative emitters characterized on metallic growth substrates, Ni, Fe and Cu. The linewidth and background of characterized emitters decreases from Ni to Fe to Cu, resulting from the increasing oxygen intercalation to the metal surface in the same order.

In addition to the narrow ZPL energy distribution, the density of emitters in the as-grown films is high and uniform, displaying similar values across subsequent growths. This is critical for device scalability and integration. For instance, the high density of quantum dots (>10 per μm^2) in GaAs/InGaAs wafers has enabled coupling of single dots to photonic crystal cavities owing to the high probability of spatial overlap between an emitter and a fabricated cavity.[28] In our

experiments, the emitter density was probed by confocal photoluminescence (PL) imaging. Figure 3a is a 5×5 μm^2 confocal map of the sample. Red and green circles indicate the locations of ensembles and single emitters, respectively. The quantum nature of SPEs was confirmed by recording the second-order autocorrelation function, $g^2(\tau)$. Figure 3b shows representative $g^2(\tau)$ measurements for ten emitters in the area mapped in figure 3a. In all cases, the intensity at zero-delay time, $g^2(\tau = 0)$, is below 0.5, confirming the quantum nature of the emission. Note that the $g^2(\tau)$ curves in figure 3b are not background-corrected, or spectrally filtered—this is deliberate to showcase the high purity of the SPEs and their suitability for practical devices. Our results show, across all characterized samples, an overall density of 2.2 emitters/μm^2 and a single emitter density of 0.84 emitters/μm^2 (figure 3c). Both values constitute significant improvements over previously published results on emitter densities in hBN,[11,26] including in commercially-available sources. To further confirm the SPE uniformity and density, images of the hBN CVD samples were taken using a wide-field EMCCD setup (figure 3d). It is impossible, however, to determine the number of single emitters using this technique. We also compared our CVD hBN with several other common types of hBN used as SPE sources (figure 3d-g). The density of SPEs is an order of magnitudes higher, constituting a vast improvement over other available hBN samples.

Furthermore, the emitters in our films are not concentrated preferentially or exclusively at grain boundaries or other large-scale defects (figure 3d)—a characteristic that is typical of exfoliated hBN flakes, where the emitters decorate straight lines (figure 3e).[29] The emitter density is also higher than other commercially available multilayer and monolayer CVD materials (figure 3f, g). This is a substantial advantage for incorporation of the emitters in devices. Furthermore, the narrow ZPL energy distribution suggests that the growth conditions favor the incorporation of a particular type of defect—in contrast to the majority of other hBN samples studied to date, which exhibit broad ZPL energy distributions and are likely the result of multiple defect species. While the chemical/atomic structure of the emitters is still a matter of much debate,[30,31] the samples grown using LPCVD offer a promising avenue to shine light on the problem. This is because the SPE energy distribution in our nominally-undoped samples is narrow, and the growth conditions that affect defect formation energies can be controlled during LPCVD growth.
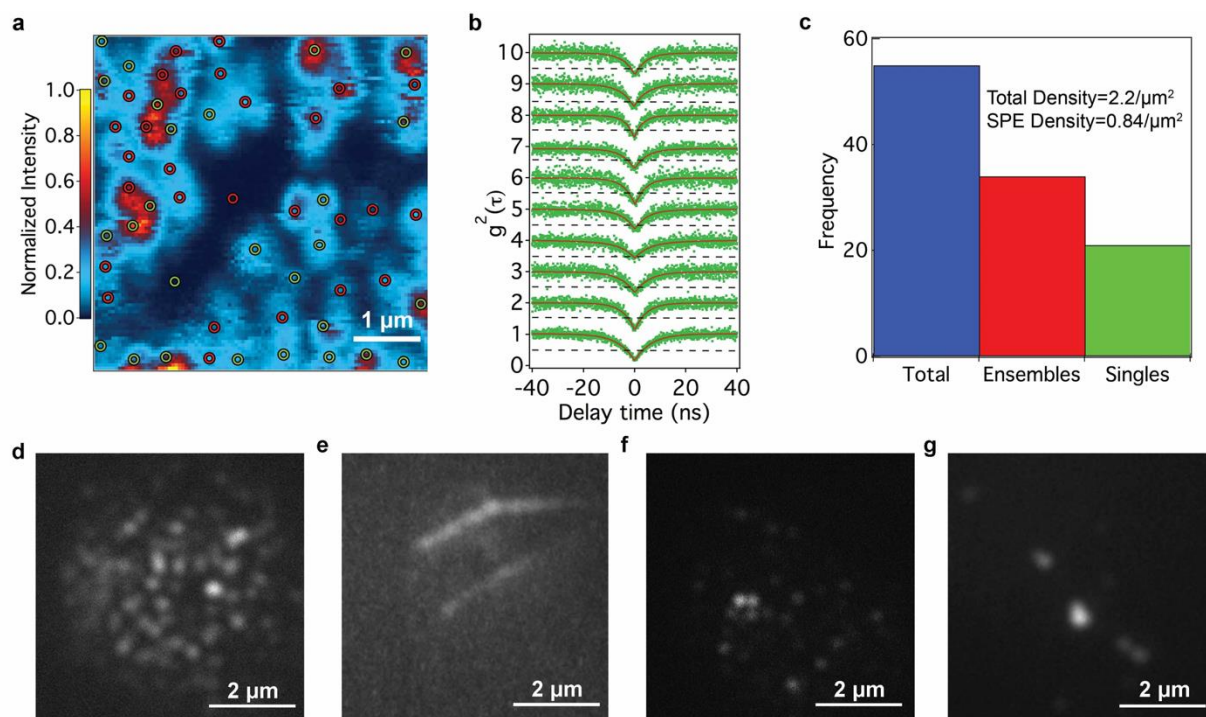
Figure 3 | Single photon emitter density in our CVD hBN films and comparison with traditional hBN sources. a. *A confocal photoluminescence map of a 5×5 µm^2 area where 55 emitters were characterized.* ***b.*** *Characteristic autocorrelation measurements of ten SPEs within the scanned region: the dashed lines indicate the 0.5 threshold (g^2(0) ≤ 0.5) for single photon emitters. The curves are not corrected for background luminescence, nor spectrally filtered during the measurement. The plots are offset vertically for display purposes.* ***c.*** *Histogram of the characterized emitters displaying the total (blue bar), ensemble (red bar), and single (green bar) photon emitter occurrence frequencies found in the confocal scan. The overall emitter densities are 2.2 emitters/µm^2 and 0.84 single emitters/µm^2.* ***d-g.*** *Wide-field EMCCD imaging of hBN sources. Scale bar: 2 µm.* ***d.*** *CVD hBN grown using the conditions described in this work, showing a high density of emitters that was uniform across the sample.* ***e.*** *Tape exfoliated hBN flakes showing regions of high emitter density at the grain boundaries. No emitters were observed inside the flat region of the flake.* ***f.*** *Commercial CVD-grown 'multilayer hBN' purchased from Graphene Supermarket, showing a lower density of emitters despite a large hBN thickness corresponding to approximately 45 monolayers of material.* ***g.*** *CVD-grown monolayer hBN purchased from Graphene Supermarket, showing a sparse density of emitters.*

The LPCVD material surpasses many of the practical limitations of other available hBN sources. For instance, commercially-available hBN material in the form of small flakes, currently the most studied hBN samples, are usually drop-casted onto substrates, which results in random dispersion. Tape-exfoliated hBN from crystal sources results in unreliable thicknesses and highly nonuniform emitter distributions that are concentrated at flake edges, wrinkles and grain boundaries. Previous studies of thin hBN layers, down to monolayers, suffered from a low concentration of emitters and emission instability.[8,32] To demonstrate the advantages of the SPEs

in our CVD-grown hBN, we realize optoelectronic devices that can be used to tune the emission frequency of hBN SPEs—an imperative step for integrated on-chip technologies.

The devices are based on two different electrolytes: polyethylene oxide mixed with lithium perchlorate (PEO:LiClO$_4$) and 1-butyl-3-methylimidazolium hexafluorophosphate (BMIM-PF6). PEO:LiClO$_4$ has been used widely for 2D materials systems with exceptional performance, owing to a strong electric field derived from a charge double-layer at the interface.[33] Meanwhile, BMIM-PF$_6$ has been shown to be effective at mediating photocarrier transfer in the absence of an applied bias, and is used here as a control system.[34]

Figure 4a shows a schematic diagram of the device structure used to control the PL emission from SPEs in few-layer LPCVD-grown hBN. The CVD hBN was transferred onto the gold electrode using a PMMA-assisted transfer method. A second electrode serves as a gate electrode. All tuning experiments utilized only emitters with a measured $g^2(0)$ of less than 0.5, and stable ZPLs that did not exhibit spectral diffusion comparable to the magnitude of the demonstrated tuning ranges.

Figure 4b shows a PL spectrum of an SPE with a ZPL at ~622 nm acquired under biases ranging from –6V to +6V. The PL was collected continuously every 10 s for 200 s at each voltage, and no spontaneous spectral jumps were observed. When the voltage was changed gradually from 0 to +6V (in steps of 2 V), the ZPL blue-shifted to ~615 nm, whilst switching the voltage to –6V caused the ZPL to red-shift to ~630 nm. Broadening of the ZPL under negative bias and narrowing under positive bias are also evident in the spectra. Overall, this SPE exhibited a continuous ZPL shift of over 15 nm when the voltage was changed from –6 V to +6 V. Such controllable tuning of SPE wavelength is the largest obtained to date from any solid state SPE.[21,23]

Next, we demonstrate dynamic modulation of a different SPE using a ±3 V square wave with a period of 200 s. The resulting ZPL wavelength modulation is shown in figure 5a. A gate voltage of +3V induces a gradual red shift from 573 nm to 580 nm over the 100 s half-cycle, and reversing the bias polarity causes the emission to gradually blue shift back to ~573 nm. Figure 5b displays corresponding changes in the FWHM of the emitter, showing a periodic broadening (narrowing) of the peak under positive (negative) gate bias, spanning a total of approximately 5 nm. The slight increase in FWHM observed on the third cycle results from the strong adsorption of hydrocarbons to hBN which causes inefficient depopulating of the trapped ions after a few cycles.[35] After the tuning experiment, the ZPL was stable, as it is demonstrated in figure 5c by a plot of ZPL wavelength *versus* time measured using a gate bias of 0 V. The spectrum was recorded for 300 s and shows that spectral drift was negligible over the time scale of the experiment, confirming that the observed modulation seen in figure 5a was induced by the applied bias. We note, however, that both the effect of the bias and the degree of reversibility varied for different SPEs, and we found no discernible trend relating the ZPL energy of emitters and the observed shifting behavior. For example, in figure S6, different emitters exhibit both red and blue shifts under a positive gate bias, and most of the shifts are unidirectional with respect to bias polarity—that is, both positive and negative biases cause a ZPL shift in the same direction, with magnitudes of up to 9 nm. In general, the shifts persist for hours after the laser is blocked and the gate bias is set to 0 V. A fraction of the emitters do not show any ZPL shifts in response

to the applied gate bias, as is explained below. The modulation time constant also varies from emitter-to-emitter and can be in the range of tens of seconds, which is not adequate for real-time correction of spectral diffusion.
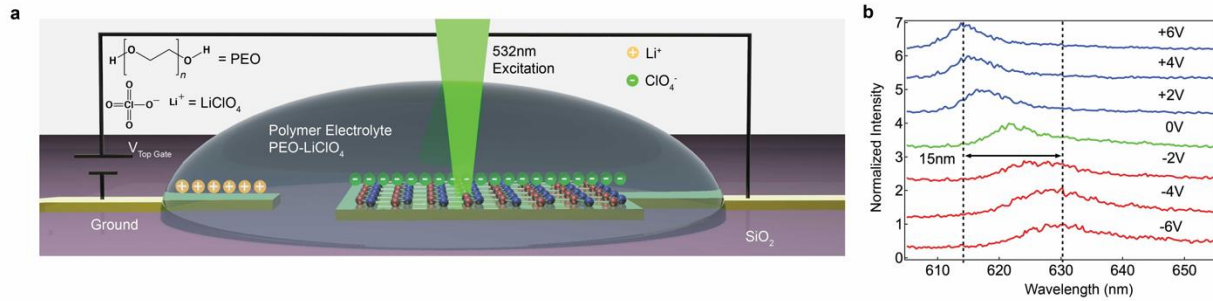
Figure 4 | Electrically-controlled optical emission in hBN with a PEO:LiClO₄ device. a. *A schematic of the electrical device used to modulate the single photon emission.* **b.** *Normalized PL spectra of a SPE at gate voltages noted displaying a shift of 15 nm. Each spectrum was collected for 10 seconds; the spectra are offset for clarity.*
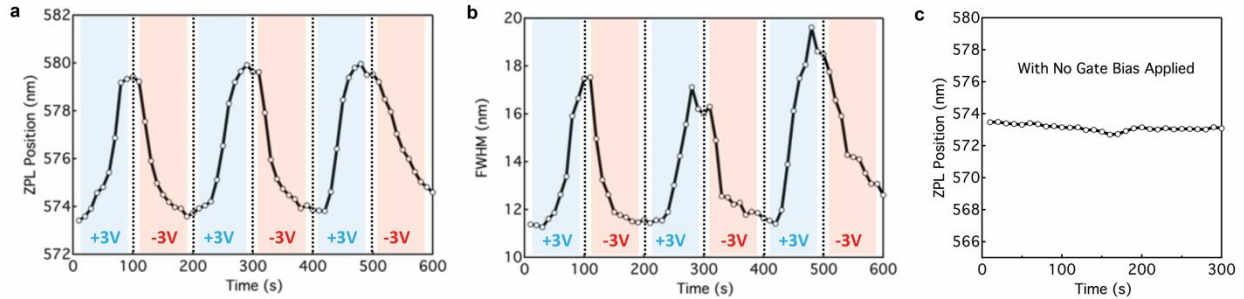

Figure 5 | Dynamic and reversible peak shifting of hBN SPE. a. *Dynamic and reversible modulation a SPE ZPL by ~7 nm, where the emitter red shifts in response to a +3 V gate bias recorded over a 100 second interval, before returning to its original position upon the switching of the gate bias to –3 V for a subsequent 100 s acquisition.* **b.** *The same SPE as in a, displayed to show the dynamic changes in the FWHM of the SPE peak which mirror the ZPL shifts observed in a.* **c.** *The same emitter as in a which displays a stable ZPL position after the gate bias has been terminated. The acquisition was performed for 300 seconds.*

The above results are consistent with a field-assisted photodoping mechanism,[34,36] where Stark shifts are induced by photocarriers that are injected into hBN and trapped at defects located in close proximity to the emitters. The observed variations in emitter behavior are attributed to corresponding variations in trap depth, type (electron or hole) and spatial/density distributions with respect to SPEs. In addition, photochemical modification of hBN may account for some irreversible changes in ZPL properties, but cannot adequately account for our results since most of the observed effects exhibit either complete or partial reversibility.

Consistent with the observed changes in ZPL FWHM, the electrolyte can also be used to stabilize spectral diffusion and blinking of emitters. Time-resolved PL spectral traces and plots of ZPL intensity vs time are shown in figure 6. At 0 V (top panels), this particular emitter exhibits random spectral jumps and intensity fluctuations, consistent with prior studies of emitters in hBN.[10,26] However, a gate bias of +2 V (middle panels) suppresses both the spectral

wondering and the blinking, and this beneficial effect on the emitter persists even after the bias is re-set to 0 V (bottom panels). This is consistent with the above model as it suggests that the device modifies the population dynamics of charge traps in the vicinity of the emitter, and demonstrates that our devices can be used to alter the local dielectric environment and stabilize blinking emitters.
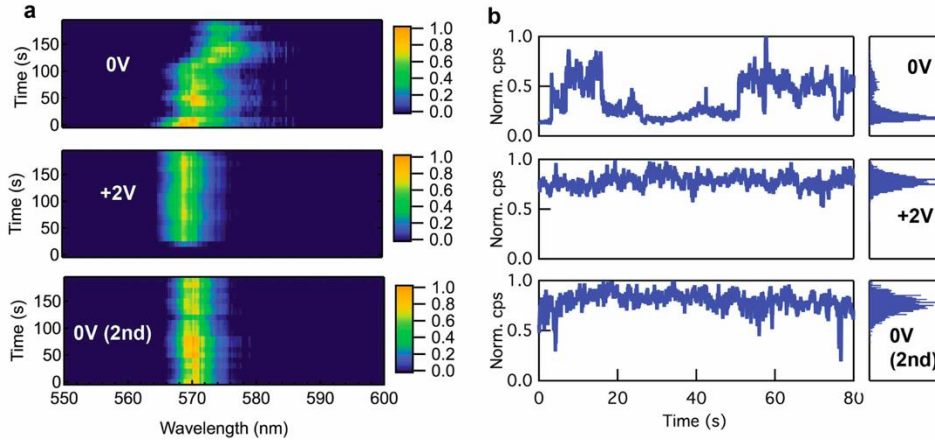
Figure 6 | Bias induced emitter stability. a. Time-resolved PL spectra collected at gate voltage series of 0,+2, 0 V, utilizing a 200-uW, 532-nm CW laser. The blinking and spectral wandering of the peak is lessened by the application of a gate voltage; this stability is maintained upon removal of the bias. b. The stabilizing effect of the same gate bias cycle as shown with normalized APD counts each shown over a period of 80 seconds. The two measurements were performed back to back for each gate voltage by utilizing a flip mirror in the confocal setup.

Finally, we performed control experiments using the BMIM-PF6, electrolyte.[33] Figure 7a shows the molecular structure of this electrolyte, and a schematic of the device configuration. The principal difference between devices based on PEO:LiClO$_4$ and BMIM-PF6 is that a gate bias is not needed to modify SPEs in the case of BMIM-PF6. This is illustrated by the PL spectra shown in figure 7b, 7c where an SPE red-shift by 17 nm and blue-shift by 15 nm, respectively, are observed under 532-nm excitation (200 uW) and zero gate bias. These large magnitude shifts display unidirectional magnitudes up to 17nm within the localized ZPL region of 580 ± 10 nm. These shifts occurred faster than those observed using the PEO:LiClO$_4$ device, with the shift in figure 7c having occurred in just over 20 seconds, however, emitters investigated using this device configuration tended to blech quickly, as the photodoping kinetics were not controlled with a gate bias. A comparison of the devices based on BMIM-PF6 and PEO:LiClO$_4$ illustrates the difference in tuning caused purely by photodoping and by field-assisted photodoping, respectively.
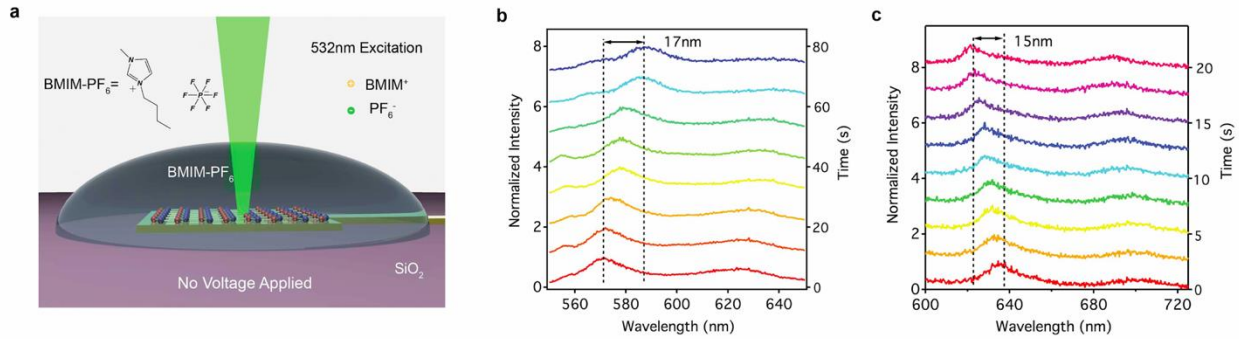
Figure 7 | ZPL shifting with BMIM-PF$_6$ due to photoinduced electron transfer. a. *Schematic of the BMIM-PF$_6$ ionic liquid device.* ***b.*** *A gradual 17-nm red shift is observed by 200-uW, 532-nm CW illumination to the sample, there is no gate voltage applied to induce this effect. In this case the electrons are liberated from the ionic liquid by the laser excitation alone using a $\lambda_{exc} = 532$ nm illumination source at 200 uW. The spectra are collected for 10 seconds each during a time-resolved PL measurement and offset for clarity. The time axis maps the collection time of the spectra displayed.* ***c.*** *A red shift of 15 nm from another SPEs is observed under the same experiment condition. All spectra were collected at 1 second acquisition times, showing the rapid kinetics of the shift observed.*

Our method for tuning of hBN SPEs offers distinct advantages over alternative techniques. First, the magnitude of the maximum observed ZPL shifts exceeds all others reported in the literature. Second, the photocarrier transfer mechanism requires the simultaneous application of a gate bias and a laser, and can therefore be used to tune individual emitters in a single device with a spatial resolution defined by the laser spot diameter. The primary drawback of the method is the variability in the response of different SPEs to the tuning stimulus due to the reliance on the nature and proximity of defects surrounding the SPEs. However, this problem is technological rather than fundamental, and is not limited to our tuning method—it is, in fact, present in all existing examples of tuning of emitters in 2D materials.[21-23] The electrolyte tuning approach is therefore competitive and appealing relative to other tuning methods.

Conclusions
In summary, we have demonstrated a robust LPCVD method for the production of centimeter-scale, few-layer hBN with stable, bright and high-quality SPEs on copper, nickel and iron substrates. The emitters are uniformly distributed in an almost atomically-thin hBN layer, and exhibit emission lines predominantly at (580 ± 10) nm, thus solving one of the most critical issues for hBN SPEs, and suggesting the preferential formation of a particular structural defect responsible for the emission. We further demonstrated controlled tuning of the emission wavelength, and stabilization of blinking SPEs using electrolyte-based devices. We proposed a photodoping model that explains our experimental results and used the devices to realize dynamic manipulation of individual emitters with nanoscale spatial resolution, over a spectral range of nearly 50 meV, all of which is possible only with high quality, few-layer, large-area hBN films. We envision that these device geometries can be further adapted for other 2D materials systems to advance progress of scalable quantum opto-electronic and nanophotonic technologies based on 2D materials.

Methods/Experimental

Chemical vapor deposition of few-layer hBN films on metal substrates: Growth was performed using a low-pressure CVD (LPCVD) technique in a ceramic tube furnace (Labec HTF50/12) with a 50-cm long heating zone. Mass flow controllers were used to meter the flow of Ar and forming gas (Ar/H$_2$, 5%) gas respectively. The system was evacuated by an oil-free scroll pump attached to the quartz tube (Advalue Technologies) with a diameter of 36 mm. The pumping speed was controlled by a throttle valve to control the growth pressure. The system has a base pressure of ~0.05 mTorr. The precursor, ammonia borane (BH$_3$NH$_3$), was stored in a high-temperature, stainless steel ampule (Swagelok), and isolated from the growth chamber by a shutoff valve prior to the growth period. Medium-porosity filters (Fisherbrand, qualitative P5) were placed above the precursor vessel to prevent transport of ammonia borane nanoparticles into the growth chamber. The precursor (and gas delivery line leading to the tube) was heated using a resistive heating belt to 95 ˚C during growth.

Cu (0.25-mm thick, 99.8%-purity Cu foils (Sigma-Aldrich)), Ni (0.125 mm, 99.9% purity (Sigma-Aldrich)), and Fe (0.1 mm, 99.9% purity (Sigma-Aldrich)) were smoothed by polishing with a commercial metal polisher (Brasso) for ~15 min prior to growth. This step not only provides a smoother growth surface, but also removes residual oxide layers from the surface. Next, the polished substrates were sonicated first in a dilute HCl solution, and then in acetone and isopropyl alcohol for 15 min each, and subsequently blow dried with N$_2$. The substrates were immediately placed in a quartz boat which was positioned in the middle of the furnace after cleaning. The precursor vessel was placed 25 cm away from the heating zoon, giving a total distance of ~50 cm between the precursor and the growth substrates. The precursor, which was stored under dry nitrogen, was loaded into the ampule 10 min after the entire CVD system reached base pressure. After that, the precursor ampule was backfilled with Ar to the desired growth pressure (2.0 Torr) before sealing from the tube prior to system purging.

The system was then purged with argon (99.999%) for at least 30 min at a flow rate of 500 sccm. The temperature was ramped up to 1030 ˚C at a rate to 20 ˚C/min under a constant flow of 300 sccm Ar/H$_2$ (5% H$_2$) at a pressure of ~1.2 Torr. Once the growth temperature was reached, the metallic foil was annealed for 2 hours (1030 ˚C, 300 sccm Ar/H$_2$, 1.2 Torr) prior to growth. To coincide with 2 hours of annealing, the precursor was heated at a rate of 10 ˚C/min to 95 ˚C. Prior to growth, the pressure was adjusted to 2.0 Torr, and the gas flow rate changed to 50 sccm Ar/H$_2$. Growth was then performed for 1 hour using a fixed pumping rate. After the growth period, the precursor isolation valve was shut off, and the gas flow was changed to 50 sccm Ar/H$_2$ and 500 sccm Ar while maintaining a pressure of 2 Torr. The growth substrates were allowed to cool slowly from 1030 ˚C to 650 ˚C at a rate of 5 ˚C/min, before being moved down the runners of the furnace to cool rapidly from 650 ˚C to room temperature under an Ar flow rate and pressure of 500 sccm and 2 Torr, respectively. Once at room temperature, the samples were removed from the quartz tube.

Transfer of hBN films: The as-grown hBN was spin-coated with PMMA (Microchem A3) at 2500 rpm for 1 min to form a ~200-nm thick PMMA film and then baked on a hotplate at 90 ˚C for 3 minutes to increase adhesion between the hBN and the polymer film. The substrate was then placed in a 0.5-M solution of ammonium persulfate to etch away the metal. After the PMMA/hBN film was detached from the metal substrate, it was then washed first in dilute HCl,

before being washed with Milli-Q water three times, and subsequently picked up on the desired substrate. The transferred film was then placed on a hot plate at 100 ˚C for 10 min, to promote adhesion of the hBN to the substrate, before the PMMA was washed away using acetone on a spin coater. Occasionally, when required to ensure complete removal of PMMA, the substrate was baked in a tube furnace (Lindberg/Blue M 50/60) using a quartz tube dedicated to PMMA oxidation at 550 ˚C in air for 2 hours to remove any residual PMMA.

Optical studies of hBN single photon emitters: PL studies were carried out using a home-built scanning confocal microscopy with continuous wave (CW) 532-nm laser (Gem 532, Laser Quantum Ltd.) as excitation. The laser was directed through a 532 nm line filter and a half-waveplate and focused onto the sample using a high numerical aperture (100x, NA = 0.9, Nikon) objective lens. Scanning was performed using an X−Y piezo fast steering mirror (FSM-300). The collected light was filtered using a 532-nm dichroic mirror (532 nm laser BrightLine, Semrock) and an additional long pass 568-nm filter (Semrock). The signal was then coupled into a graded-index multimode fiber, where the fiber aperture of 62.5 μm serves as a confocal pinhole. A flipping mirror was used to direct the emission to a spectrometer (Acton Spectra Pro, Princeton Instrument Inc.) or to two avalanche photodiodes (Excelitas Technologies) in a Hanbury Brown-Twiss configuration, for collection of spectra and photon counting, respectively. Correlation measurements were carried out using a time-correlated single photon counting module (PicoHarp 300, PicoQuant). All the second-order autocorrelation $g^2(\tau)$ measurements were analyzed and fitted without background correction unless otherwise specified. The same time-tagging module was used in conjunction with a supercontinuum laser (Fianium WhiteLase) to perform time-resolved PL measurements.

Wide-field EMCCD imaging of hBN: Quantum emitters in various hBN samples were recorded on a EMCCD camera with an exposure time of ~200 ms for 100 acquisitions. Excitation was done with a continuous wave 532-nm laser using a power of 3 mW, recording an area of approximately 5×5 μm^2. Video file showing the region of CVD hBN in figure 3d is included in external supplementary information file.

Polymer Electrolyte Devices: To make the gold electrodes, silicon substrates with a 300-nm thick thermal oxide layer were patterned with standard optical lithography followed by sputter deposition of 5/25 nm Ti/Au. The hBN film prepared with CVD was transferred onto the gold electrodes using the PMMA-assisted transfer method as mentioned above. PMMA film was removed using a hot acetone bath (50 ˚C, 30 min), followed by rinsing with IPA and deionized water. The samples were baked at 100 ˚C for 30 min prior to coating with the electrolytes. The polymer electrolyte—comprised of polyethylene oxide (PEO, Mw ~10,000) and $LiClO_4$ (1:0.12, w/w), was dissolved in acetonitrile and filtered with a polytetrafluoroethylene syringe filter (pore size 0.2 um))—was spin-coated on top of hBN at 2500 rpm and dried for 30 min in air at 40 ˚C on a hotplate. 1-butyl-3-methylimidazolium hexafluorophosphate ($BMIM\text{-}PF_6$) was also used, and the devices were prepared in the same way, with the exception of the drying step which was not performed in the case of $BMIM\text{-}PF_6$. For the modulation measurements, a source meter unit (Keithley 2601) was used to bias the device while a long working distance objective (NA 0.7) was used for PL measurements of the devices. In devices utilizing $PEO\text{:}LiClO_4$, the emitters' ZPLs are stable under continuous excitation with a 532-nm, 200–300-uW laser. Similarly, the ZPL wavelengths and widths do not change when the emitters are kept in dark and a gate voltage

is applied. This illustrates that, in the case of the PEO:LiClO4 devices, the effects discussed below require simultaneous application both of a bias and a laser pump.

Author contributions
I.A., M.T., Z.X. and N.M. conceived the project. N.M. carried out the CVD growth of hBN, performed the structural and optical characterization of the hBN quantum emitters with assistance from T.T., and C.B. The CVD system was designed by N.M and J.S. I.A. and M.T. supervised the project. Z.X. and N.M designed and conducted the spectral modulation experiment. N.M. performed all data analysis in this work together with Z.X and T.T. All authors discussed the results and co-wrote the manuscript.

Associated Content
Information detailing procedures, equations, and fittings utilized. Additional photophysical characterization of emitters, FTIR and Raman spectroscopy for all growths performed, additional AFM traces, a CVD system schematic, and further tuning results.

References
1 Atatüre, M., Englund, D., Vamivakas, N., Lee, S.-Y. & Wrachtrup, J. Material Platforms for Spin-Based Photonic Quantum Technologies. *Nat. Rev. Mater.* **2018**, 3, 38-51.
2 Awschalom, D. D., Hanson, R., Wrachtrup, J. & Zhou, B. B. Quantum Technologies with Optically Interfaced Solid-State Spins. *Nat. Photonics* **2018**, 12, 516-527.
3 Senellart, P., Solomon, G. & White, A. High-performance Semiconductor Quantum-Dot Single-Photon Sources. *Nat. Nanotechnol.* **2017**, 12, 1026-1039.
4 Aharonovich, I., Englund, D. & Toth, M. Solid-State Single-Photon Emitters. *Nat. Photonics* **2016**, 10, 631-641.
5 Kalb, N.; Reiserer, A. A.; Humphreys, P. C.; Bakermans, J. J. W.; Kamerling, S. J.; Nickerson, N. H.; Benjamin, S. C.; Twitchen, D. J.; Markham, M.; Hanson, R., Entanglement Distillation Between Solid-State Quantum Network Nodes. *Science* **2017**, 356, 928-932.
6 Chu, X.-L., Götzinger, S. & Sandoghdar, V. A Single Molecule as a High-Fidelity Photon Gun for Producing Intensity-Squeezed Light. *Nat. Photonics* **2016**, 11, 58-62.
7 He, X.; Htoon, H.; Doorn, S. K.; Pernice, W. H. P.; Pyatkov, F.; Krupke, R.; Jeantet, A.; Chassagneux, Y.; Voisin, C., Carbon Nanotubes as Emerging Quantum-Light Sources. *Nat. Mater.* **2018**, 17, 663-670.
8 Tran, T. T., Bray, K., Ford, M. J., Toth, M. & Aharonovich, I. Quantum Emission from Hexagonal Boron Nitride Monolayers. *Nat. Nanotechnol.* **2016**, 11, 37-41.

9   Jungwirth, N. R.; Calderon, B.; Ji, Y.; Spencer, M. G.; Flatte, M. E.; Fuchs, G. D., Temperature Dependence of Wavelength Selectable Zero-Phonon Emission from Single Defects in Hexagonal Boron Nitride. *Nano Lett.* **2016**, 16, 6052-6057.

10   Shotan, Z.; Jayakumar, H.; Considine, C. R.; Mackoit, M.; Fedder, H.; Wrachtrup, J.; Alkauskas, A.; Doherty, M. W.; Menon, V. M.; Meriles, C. A., Photoinduced Modification of Single-Photon Emitters in Hexagonal Boron Nitride. *ACS Photonics* **2016**, 3, 2490-2496.

11   Exarhos, A. L., Hopper, D. A., Grote, R. R., Alkauskas, A. & Bassett, L. C. Optical Signatures of Quantum Emitters in Suspended Hexagonal Boron Nitride. *ACS Nano* **2017**, **11**, 3328-3336.

12   Sahoo, P. K., Memaran, S., Xin, Y., Balicas, L. & Gutierrez, H. R. One-Pot Growth of Two-Dimensional Lateral Heterostructures *via* Sequential Edge-Epitaxy. *Nature* **2018**, 553, 63-67.

13   Nicholas V. Proscia, Z. S., Harishankar Jayakumar, Prithvi Reddy, Michael Dollar, Audrius Alkauskas, Marcus Doherty, Carlos A. Meriles, Vinod M. Menon. Near-Deterministic Activation of Room Temperature Quantum Emitters in Hexagonal Boron Nitride. *Optica* **2018**, 5, 1128-1134.

14   Palacios-Berraquero, C.; Kara, D. M.; Montblanch, A. R.; Barbone, M.; Latawiec, P.; Yoon, D.; Ott, A. K.; Loncar, M.; Ferrari, A. C.; Atature, M. Large-Scale Quantum-Emitter Arrays in Atomically Thin Semiconductors. *Nat. Commun.* **2017,** 8, 15093.

15   Branny, A., Kumar, S., Proux, R. & Gerardot, B. D. Deterministic Strain-induced Arrays of Quantum Emitters in a Two-Dimensional Semiconductor. *Nat. Commun.* **2017**, 8, 15053.

16   Kim, K. K.; Hsu, A.; Jia, X.; Kim, S. M.; Shi, Y.; Dresselhaus, M.; Palacios, T.; Kong, J., Synthesis and Characterization of Hexagonal Boron Nitride Film as a Dielectric Layer for Graphene Devices. *ACS Nano* **2012**, 6, 8583-90.

17   Lin, W.-H.; Brar, V. W.; Jariwala, D.; Sherrott, M. C.; Tseng, W.-S.; Wu, C.-I.; Yeh, N.-C.; Atwater, H. A., Atomic-Scale Structural and Chemical Characterization of Hexagonal Boron Nitride Layers Synthesized at the Wafer-Scale with Monolayer Thickness Control. *Chem. Mater.* **2017**, 29, 4700-4707.

18   Chang, R.-J.; Wang, X.; Wang, S.; Sheng, Y.; Porter, B.; Bhaskaran, H.; Warner, J. H., Growth of Large Single-Crystalline Monolayer Hexagonal Boron Nitride by Oxide-Assisted Chemical Vapor Deposition. *Chem. Mater.* **2017**, 29, 6252-6260.

19   Song, L.; Ci, L.; Lu, H.; Sorokin, P. B.; Jin, C.; Ni, J.; Kvashnin, A. G.; Kvashnin, D. G.; Lou, J.; Yakobson, B. I.; Ajayan, P. M., Large Scale Growth and Characterization of Atomic Hexagonal Boron Nitride Layers. *Nano Lett.* **2010**, 10, 3209-15.

20   Jana, M. & Singh, R. N. Progress in CVD Synthesis of Layered Hexagonal Boron Nitride with Tunable Properties and Their Applications. *Int. Mater. Rev.* **2017**, 63, 162-203.

21   Noh, G.; Choi, D.; Kim, J. H.; Im, D. G.; Kim, Y. H.; Seo, H.; Lee, J., Stark Tuning of Single-Photon Emitters in Hexagonal Boron Nitride. *Nano Lett*. **2018**, 18, 4710-4715.

22   Xue, Y.; Wang, H.; Tan, Q.; Zhang, J.; Yu, T.; Ding, K.; Jiang, D.; Dou, X.; Shi, J. J.; Sun, B. Q., Anomalous Pressure Characteristics of Defects in Hexagonal Boron Nitride Flakes. *ACS Nano* **2018**, 12, 7127-7133.

23   Chakraborty, C.; Goodfellow, K. M.; Dhara, S.; Yoshimura, A.; Meunier, V.; Vamivakas, A. N., Quantum-Confined Stark Effect of Individual Defects in a van der Waals Heterostructure. *Nano Lett.* **2017**, 17, 2253-2258.

24   Kim, K. K.; Hsu, A.; Jia, X.; Kim, S. M.; Shi, Y.; Hofmann, M.; Nezich, D.; Rodriguez-Nieva, J. F.; Dresselhaus, M.; Palacios, T.; Kong, J., Synthesis of Monolayer Hexagonal Boron Nitride on Cu Foil Using Chemical Vapor Deposition. *Nano Lett.* **2012**, 12, 161-6.

25   Feigelson, B. N.; Bermudez, V. M.; Hite, J. K.; Robinson, Z. R.; Wheeler, V. D.; Sridhara, K.; Hernández, S. C., Growth and Spectroscopic Characterization of Monolayer and Few-Layer Hexagonal Boron Nitride on Metal Substrates. *Nanoscale* **2015**, 7, 3694-3702.

26   Li, X.; Shepard, G. D.; Cupo, A.; Camporeale, N.; Shayan, K.; Luo, Y.; Meunier, V.; Strauf, S., Nonmagnetic Quantum Emitters in Boron Nitride with Ultranarrow and Sideband-Free Emission Spectra. *ACS Nano* **2017**, 11, 6652-6660.

27   Tran, T. T.; Elbadawi, C.; Totonjian, D.; Lobo, C. J.; Grosso, G.; Moon, H.; Englund, D. R.; Ford, M. J.; Aharonovich, I.; Toth, M., Robust Multicolor Single Photon Emission from Point Defects in Hexagonal Boron Nitride. *ACS Nano* **2016**, 10, 7331-8.

28   Kim, H.; Shen, T. C.; Roy-Choudhury, K.; Solomon, G. S.; Waks, E., Resonant Interactions between a Mollow Triplet Sideband and a Strongly Coupled Cavity. *Phys. Rev. Lett.* **2014**, 113, 027403.

29   Grosso, G.; Moon, H.; Lienhard, B.; Ali, S.; Efetov, D. K.; Furchi, M. M.; Jarillo-Herrero, P.; Ford, M. J.; Aharonovich, I.; Englund, D., Tunable and High-Purity Room Temperature Single-Photon Emission from Atomic Defects in Hexagonal Boron Nitride. *Nat. Commun.* **2017**, 8, 705.

30   Abdi, M.; Chou, J.-P.; Gali, A.; Plenio, M. B., Color Centers in Hexagonal Boron Nitride Monolayers: A Group Theory and *Ab Initio* Analysis. *ACS Photonics* **2018**, 5, 1967-1976.

31   Tawfik, S. A.; Ali, S.; Fronzi, M.; Kianinia, M.; Tran, T. T.; Stampfl, C.; Aharonovich, I.; Toth, M.; Ford, M. J., First-Principles Investigation of Quantum Emission from hBN Defects. *Nanoscale* **2017**, 9, 13575-13582.

32   Ngoc My Duong, H.; Nguyen, M. A. P.; Kianinia, M.; Ohshima, T.; Abe, H.; Watanabe, K.; Taniguchi, T.; Edgar, J. H.; Aharonovich, I.; Toth, M., Effects of High-Energy Electron Irradiation on Quantum Emitters in Hexagonal Boron Nitride. *ACS Appl. Mater. Interfaces* **2018,** *10*, 24886-24891.

32   Lu, C., Fu, Q., Huang, S. & Liu, J. Polymer Electrolyte-Gated Carbon Nanotube Field-Effect Transistor. *Nano Letters* **2004**, 4, 623-627.

33   Vieira, R. C. & Falvey, D. E. Photoinduced Electron-Transfer Reactions in Two Room-Temperature Ionic Liquids: 1-Butyl-3-Methylimidazolium Hexafluorophosphate and 1-Cctyl-3-Methylimidazolium Hexafluorophosphate. *J. Phys. Chem. B* **2007**, 111, 5023-5029.

34   Ju, L.; Velasco, J., Jr.; Huang, E.; Kahn, S.; Nosiglia, C.; Tsai, H. Z.; Yang, W.; Taniguchi, T.; Watanabe, K.; Zhang, Y.; Zhang, G.; Crommie, M.; Zettl, A.; Wang, F., Photoinduced Doping in Heterostructures of Graphene and Boron Nitride. *Nat. Nanotechnol.* **2014,** *9*, 348-52.

35   Cai, Q.; Mateti, S.; Watanabe, K.; Taniguchi, T.; Huang, S.; Chen, Y.; Li, L. H., Boron Nitride Nanosheet-Veiled Gold Nanoparticles for Surface-Enhanced Raman Scattering. *ACS Appl. Mater. Interfaces* **2016,** *8*, 15630-6.

36   Wong, D.; Velasco, J., Jr.; Ju, L.; Lee, J.; Kahn, S.; Tsai, H. Z.; Germany, C.; Taniguchi, T.; Watanabe, K.; Zettl, A.; Wang, F.; Crommie, M. F., Characterization and

Manipulation of Individual Defects in Insulating Hexagonal Boron Nitride Using Scanning Tunnelling Microscopy. *Nat. Nanotechnol.* **2015,** *10*, 949-53.